On the fracture behavior of Cr$_2$AlC coatings

B. Völker [a,b,1,*], B. Stelzer [a], S. Mráz [a], H. Rueß [a], R. Sahu [a,b], C. Kirchlechner [b,2], G. Dehm [b], J.M. Schneider [a]

[a] Materials Chemistry, RWTH Aachen University, Kopernikusstraße 10, D-52074 Aachen, Germany
[b] Max-Planck-Institut für Eisenforschung GmbH, Max-Planck-Straße 1, D-40237 Düsseldorf, Germany

HIGHLIGHTS

- The fracture toughness of the amorphous Cr$_2$AlC coating is significantly higher than for the crystalline Cr$_2$AlC coatings.
- The microstructure has a minor influence on the fracture toughness of crystalline Cr2AlC coatings.
- Crystalline Cr$_2$AlC shows brittle intercrystalline fracture.

GRAPHICAL ABSTRACT
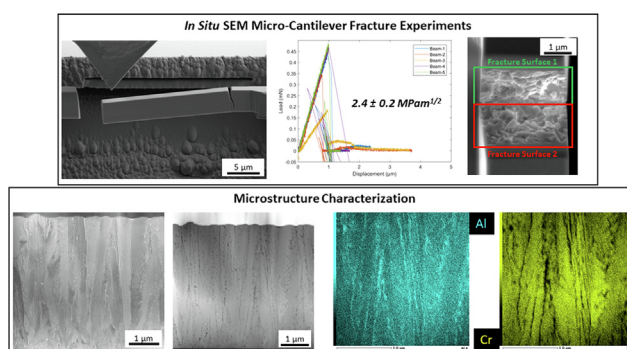
ABSTRACT

Bulk MAX phase materials were investigated heavily in the last decades due to their advantageous combination of metallic and ceramic properties. In recent years, MAX phases also gained the interest of the protective coatings community. Cr$_2$AlC is a very promising material, since the crystalline MAX phase can be deposited at comparatively low (550 °C) substrate temperatures. Another advantage of the Cr$_2$AlC MAX phase is its self-healing ability. The goal of this investigation was to characterize the fracture toughness of Cr$_2$AlC protective coatings using *in situ* SEM micro-cantilever tests and to determine the influence of different microstructures on the fracture behavior. Surprisingly, the fracture toughness is only moderately affected by the microstructure of the crystalline samples investigated here, which reveal a fracture toughness ranging from *1.8 ± 0.1 MPam$^{1/2}$* to *2.4 ± 0.2 MPam$^{1/2}$*.

In contrast to that, it could be shown that there is a significant increase in fracture toughness for the amorphous coating with identical chemical composition (*4.1 ± 0.5 MPam$^{1/2}$*) of almost twice the fracture toughness compared to the crystalline coatings. The detrimental influence of grain boundaries in the crystalline coating and the lack of grain boundaries in the amorphous sample might explain the formidable fracture toughness.

© 2021 The Authors. Published by Elsevier Ltd. This is an open access article under the CC BY-NC-ND license (http://creativecommons.org/licenses/by-nc-nd/4.0/).

1. Introduction

In the last decades, MAX phase materials were extensively investigated due to their beneficial combination of metallic and ceramic properties [1–8]. Their chemical compositions can be represented as M$_{n+1}$AX$_n$, here M is an early transition metal (e.g.: Cr,

Ti, V, Ta, Nb...), A is an A-group element (e.g.: Al, Si,...) and X is either C or N [2,3,6–8]. In general, they have a layered microstructure along the c-axis, where, depending on the configuration, different alternating MX layers are intersected by a single A layer [2]. A more detailed description of the microstructure and the resulting properties can be found in [2,7,8].

Bulk MAX phases revealed interesting property combinations of good e.g. electrical conductivity and/or ductility (metallic) in combination with improved thermal shock resistivity and/or oxidation resistance (ceramic) [3,7]. Major challenges in MAX phases research include the synthesis of single phased material at low temperatures [1,7–9].

The above discussed MAX phase property combinations underline the potential for application as protective coatings which is explored with increasing interest [6,10–17]. Early on, it was shown that MAX phase microstructures can be produced using different deposition techniques, e.g. chemical vapor deposition (CVD) or physical vapor deposition (PVD) processes [6]. To synthesize crystalline MAX phase coatings, it was necessary to use deposition temperatures up to around *900 °C* [6,10,14]. Such high temperatures limit the substrates that can be used for the deposition process. Recently, it became possible to deposit crystalline MAX phase coatings at significantly lower deposition temperatures [18,19] allowing the deposition onto technologically relevant substrate materials, e.g. steels, without degradation of the substrate properties. Cr_2AlC, one of the MAX phases, is a very promising candidate for protective coating applications as Cr_2AlC coatings form a passivating alumina layer upon oxidation [20] and Cr_2AlC shows self-healing behavior [21–23]. In previous investigations, it was shown that evolution of both, the crystal structure (disordered solid solution vs ordered MAX phase) and the microstructure (columnar vs equiaxed morphology) of Cr_2AlC coatings can be affected by the synthesis strategy adopted [24]. Specifically, post-deposition annealing treatments of the amorphous coatings resulted in the formation of equiaxed MAX phase grains [18,19]. Furthermore, it was revealed that the microstructure changes can be tracked remotely via a change in resistivity without invasive experimental methods [19].

For bulk Ti_3SiC_2 MAX phase material a decrease in fracture toughness from coarse grained (>*50 μm*) to fine grained (<*10 μm*) was observed [25]. Gilbert et al. [25] suggested that the reason for the improved fracture toughness of the coarse grained material are crack bridges, which are occurring more often in the coarse grained material, and thus, increase the measured fracture toughness. An investigation on Cr_2AlC reported, that there is a similar influence of the grain size, revealing a fracture toughness of ~ *4 MPam$^{1/2}$* for fine grained material, with a grain size of *1–3 μm,* to about ~ *6 MPam$^{1/2}$* for a coarse grained material, with a grain size of ~ *35 μm* [26]. A more recent study [27] reported a fracture toughness of ~ *8 MPam$^{1/2}$* for a grain size between *1* and *3 μm* for bulk Cr_2AlC. Another investigation on bulk Cr_2AlC reported that the fracture toughness is strongly depending on the texture of the material and can range from ~ *2 MPam$^{1/2}$* to ~ *12 MPam$^{1/2}$* for a fine grained (~*2 μm* grain size) material [28].

Therefore, it is reasonable to assume that the fracture behavior of bulk MAX phases, especially Cr_2AlC, are also affected by texture, defects and other processing induced factors [26–28]. Also it is evident that the currently available literature does not allow for a causal discussion of the impact of grain size on the fracture behavior of MAX phases.

Determining the mechanical properties of hard coatings can be very challenging due to their thicknesses of only a few *μm*, which in turn limits the available techniques. One of the most common techniques is nanoindentation, which gives an estimate of the hardness and the indentation modulus of the coating [29–31]. Another important mechanical property for hard protective coat-

ings, that is recently getting in the focus of the hard coating community due to the advancements in micro-mechanical sample preparation and testing, is the fracture toughness [32–37]. In the literature, a lot of different methods are presented to determine the fracture toughness using micro-mechanical testing [38–42]. Of these, the micro-bending cantilever method according to Matoy et al. [38] is the most established one and it is the one best suited for hard coatings. In bulk materials it was shown that the microstructure can have a pronounced influence on the fracture mechanical response of a material [43–46]. Therefore, micro-bending cantilever experiments were performed to investigate the fracture behavior of Cr_2AlC coatings and the influence of the deposition parameters on the microstructure and, hence, on the fracture behavior of the coatings.

2. Experimental

Cr_2AlC coatings were deposited in an industrial deposition chamber (CemeCon) and a laboratory deposition chamber. In Table 1, a list of the coatings is found and subsequently the deposition parameters are described in detail.

The Cr_2AlC coatings were deposited by direct current (DCMS) and high power pulsed magnetron sputtering (HPPMS) in an industrial chamber (CC800/9, CemeCon AG, Wuerselen, Germany). A powder metallurgical composite Cr:Al:C target exhibiting a stoichiometry of 2:1:1 was employed (PLANSEE Composite Materials GmbH, Lechbruck am See, Germany). *10x10x0.5 mm^3* single crystalline MgO (100) substrates (Crystal GmbH, Berlin, Germany) were kept at floating potential and were heated to *565 °C* prior to deposition. Additionally, samples were synthesized without intentional heating by DCMS. The chamber base pressure was below *0.5 mPa* for all depositions. A time-averaged power of *1000 W* resulted in a target power density of *2.3 W cm^{-2}* in case of DCMS and a target peak power density of approximately *460 W cm^{-2}* in the case of HPPMS at a frequency of *250 Hz* and a duty cycle of *1.25%*. For DCMS depositions, a substrate to target distance of *50 mm* and a deposition pressure of *0.19 Pa* were set, whereas for HPPMS depositions, the values of *75 mm* and *0.39 Pa* were used, respectively.

The DCMS$_{RT, as-dep}$ sample was deposited following the procedure described by Stelzer et al. [19].

A sample (DCMS$_{RT anneal}$) synthesized by DCMS without heating during deposition was subsequently annealed in a vertical tube vacuum furnace at *650 °C* with no holding time and a heating and cooling rate of *5 Kmin^{-1}*. The base pressure was below *0.3 mPa*.

The Cr_2AlC coating produced in the laboratory chamber (DCMS$_{lab 600°C}$) was deposited onto the same *10x10x0.5 mm^3* MgO (100) substrate by DCMS. The substrate was located at a distance of *100 mm* from a *50 mm* circular magnetron. A powder metallurgical composite Cr-Al-C target with a 2:1:1 composition (Plansee Composite Materials GmbH, Germany) was used for the deposition. The substrate was heated to *600 °C* prior to deposition as calibrated by a thermocouple. The base pressure of the deposition system with the heated substrate was approximately *0.1 mPa*. The Ar deposition pressure was *1.0 Pa*. The magnetron was powered with a DC power supply MDX *2.5 kW* (Advanced Energy, USA) operated at a constant DC power of *200 W*. The substrate was kept electrically floating.

The Cr_2AlC coating for the electron energy loss spectroscopy (EELS) investigation was deposited on a single crystalline Al_2O_3 (0001) substrate using DCMS with similar deposition parameters as the DCMS coatings deposited onto MgO described above.

The thickness of all the deposited coatings was approximately *4 μm*.

Table 1
List of deposited Cr_2AlC coatings. Direct current magnetron sputtering (DCMS); High power pulsed magnetron sputtering (HPPMS); without intentional heating (RT).

Deposition Chamber	Deposition Process	Substrate Temperature	Annealing Temperature	Sample Name
CemeCon	DCMS	565 °C	–	$DCMS_{565°C}$
Laboratory Chamber	DCMS	600 °C	–	$DCMS_{lab,\ 600°C}$
CemeCon	HPPMS	565 °C	–	$HPPMS_{565°C}$
CemeCon	DCMS	RT	–	$DCMS_{RT,\ as\text{-}dep}$
CemeCon	DCMS	RT	650 °C	$DCMS_{RT,\ anneal}$
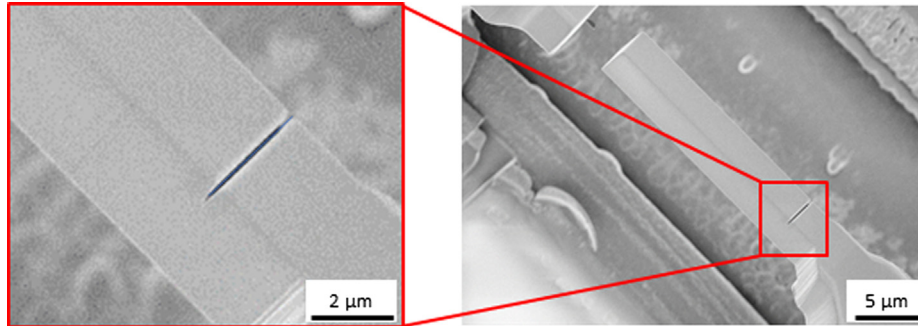
Fig. 1. In a) a detailed view of a through thickness notch is shown and b) depicts an overview image of a micro-bending cantilever. The notch is made into the surface of the deposited coatings.

Microstructural and chemical characterization was done using focused ion beam (FIB) lift out transmission electron microscope (TEM) samples, which were prepared using a Thermo Fisher Scientific dual beam "Scios 2 HiVac" system. STEM bright field (BF) and high-angle annular dark field (HAADF) images were taken on a JEOL 2200FS TEM with an acceleration voltage of *200 kV*, equipped with a *100 mm²* energy dispersive X-ray (EDX) detector from JEOL.

A qualitative phase analysis of the $DCMS_{565°C}$, $DCMS_{lab,\ 600°C}$, $HPPMS_{565°C}$ and the $DCMS_{RT,\ anneal}$ samples was done using X-ray measurements on a Seifert Type ID3003 with a Huber 4- Circle + XYZ goniometer and a Co-source with *40 kV / 30 mA* power setup. As a detector, a Meteor0D – energy dispersive point detector was employed. The beam diameter was around *1 mm*. A step width of *Δ2Θ* of *0.05°* and a count time per step of *5 s* were used.

Cantilevers from the center region of the coated MgO wafers were prepared using an Auriga dual beam Ga-ion FIB from Zeiss with a *30 kV* acceleration voltage. The cantilevers were machined with a cross section of around *3.5 μm × 3.5 μm* and the length of the cantilevers was chosen so that the distance between the indenter and the notch could be at least five times the height of the beam, to be sure that predominantly mode I loading is occurring, as proposed by Brinckmann et al. [47]. Coarse cutting was done with a Ga current of *16 nA* and *2 nA* and final polishing with a current of *240 pA*. The notch was made using a current of *50 pA* with a distance from the base of the beam similar to the height to prevent any influence during loading from the fixed end of the beam. An overview SEM image of a beam is depicted in Fig. 1b and a detailed view of the through thickness notch is shown in Fig. 1a.

The *in situ* cantilever tests were performed in a Gemini500 SEM from Zeiss using an ASMEC UNAT2 *in situ* indenter with a loading rate of *20 nm/s*. For each coating microstructure, at least five bending beams were tested. The evaluation was performed according to Matoy et al. [38] with the following equations for the geometry factor f(a/W) and K_Q.

$$f\left(\frac{a}{W}\right) = 1.46 + 24.36\left(\frac{a}{W}\right) - 47.21\left(\frac{a}{W}\right)^2 + 75.18\left(\frac{a}{W}\right)^3 \tag{1}$$

$$K_Q = \frac{F_{max}L}{BW^{\frac{3}{2}}}f\left(\frac{a}{W}\right) \tag{2}$$

Here, *a* is the notch depth and *W* is the height of the beam. F_{max} is the load at fracture of the cantilever, *B* the width of the sample and *L* the distance between notch and indenter tip.

To determine if the measured K_Q is a sample size independent mode I fracture toughness (K_{IC}), the criteria according to ASTM standard E399-90 for macroscopic testing [48] were used. At first, all the samples should show a linear elastic load–displacement curve and, secondly, the minimum required sample size requirements need to be met. The minimum required sample dimensions were calculated according to following formula:

$$a, B, W - a \geq 2.5\left(\frac{K_Q}{\sigma_y}\right)^2 \tag{3}$$

Nanoindentation measurements were performed on a Hysitron TI 950 Tribometer equipped with a Berkovich diamond tip to determine the hardness values of the coatings. The yield strength is therefore very roughly estimated according to Eq. (4), the rule of thumb from Tabor [49], who developed this method for steel.

$$\sigma_y[GPa] = \frac{Hardness[GPa]}{3} \tag{4}$$

For the electron energy loss spectroscopy (EELS) measurement, a cross section TEM lamella of Cr_2AlC on single crystalline Al_2O_3 was prepared using a Thermo Fisher Scientific dual beam "Scios 2 HiVac" FIB. The high angle annular dark field (HAADF) imaging and EELS in scanning transmission electron microscopy (STEM) were conducted with a Gatan GIF Quantum ERS energy filter on a probe-corrected Thermo Fisher Scientific Titan Themis STEM at *300 kV* acceleration voltage. During EELS acquisition, the energy resolution was set to *1 eV* and the spectra were recorded using a *5 mm* aperture at a dispersion of *0.10 eV* per channel.

3. Results

All Cr_2AlC coatings deposited at elevated substrate temperature had a columnar microstructure, as shown by the STEM BF-images in Fig. 2a–c. In addition, the images indicate a brighter contrast at the grain boundaries, as can be seen in Fig. 2a-c. For the $DCMS_{RT,\ as-dep}$ sample, the STEM investigations revealed an amorphous
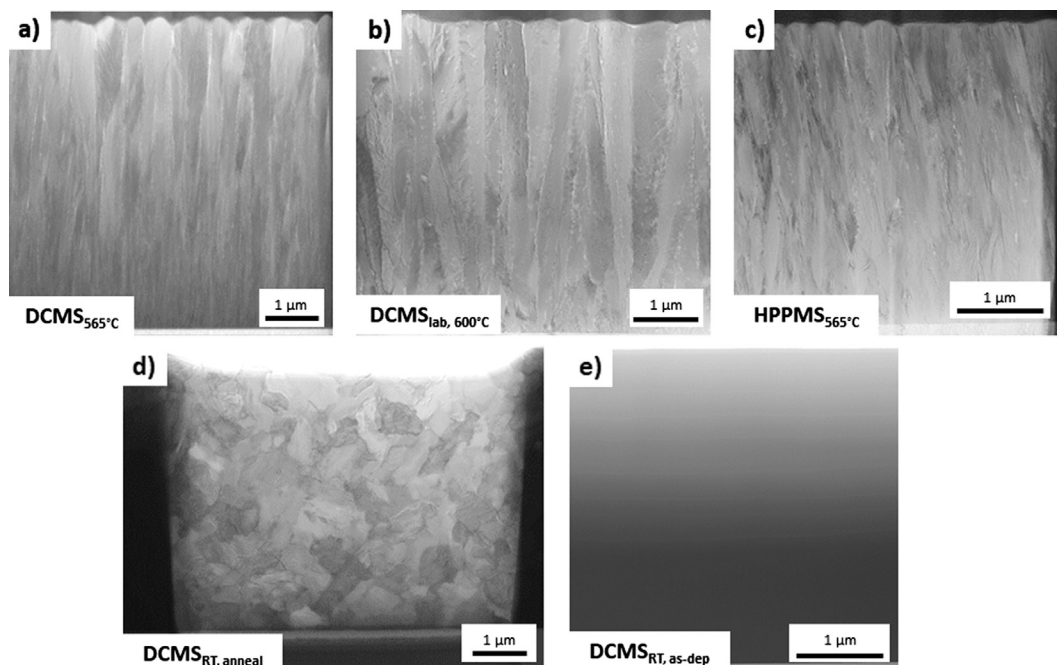
Fig. 2. In a)-c) the STEM BF images of the Cr$_2$AlC coating deposited at elevated substrate temperatures, a) DCMS$_{565°C}$, b) DCMS$_{lab, 600°C}$ and c) HPPMS$_{565°C}$, are depicted. All samples show a more or less elongated microstructure, which is common for sputtered coatings, with bright contrast features at the grain boundary. d) and e) depict the samples deposited without intentional heating. In d) the sample with the subsequent heat treatment at 650 °C is shown. It has an equiaxed microstructure without any features at the grain boundary. In e) the sample shows no microstructural features, which is indicative of an amorphous microstructure.
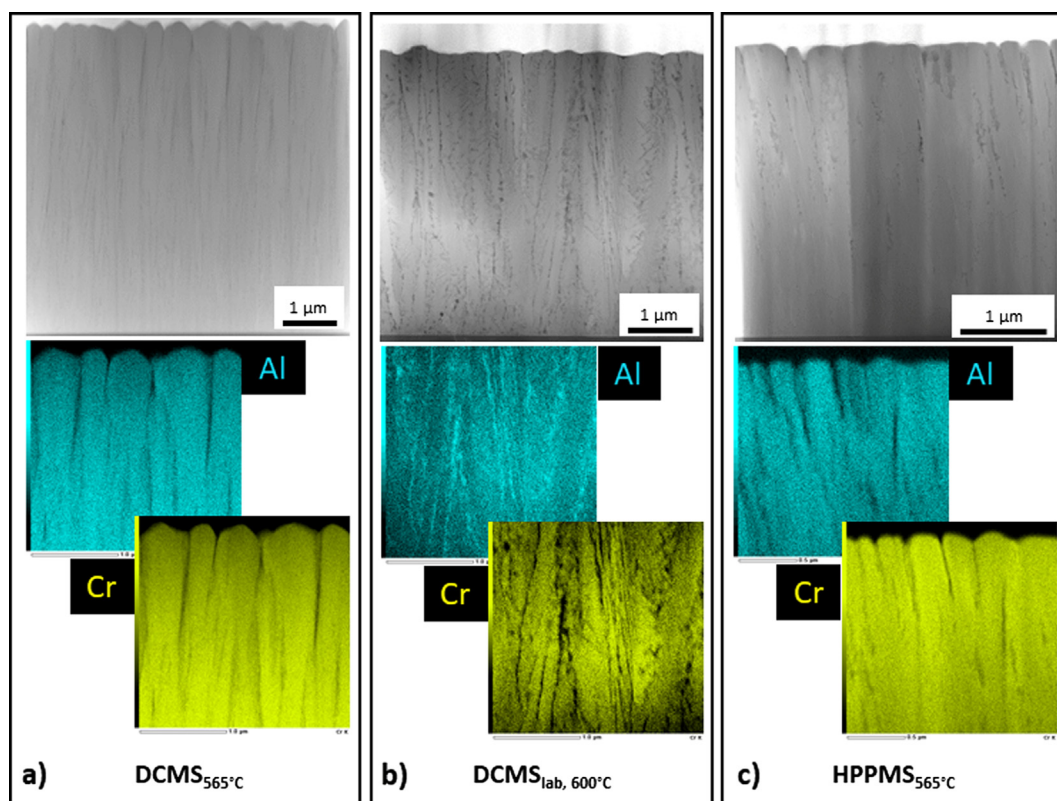

Fig. 3. a)–c) depict HAADF STEM images of the DCMS$_{565°C}$, DCMS$_{lab, 600°C}$ and HPPMS$_{565°C}$ samples with corresponding EDX maps of Al and Cr, respectively. a) and c) clearly reveal pores at the grain boundary for the DCMS$_{565°C}$ and HPPMS$_{565°C}$ sample. For the HPPMS$_{565°C}$ sample, pores are only found in the upper half of the coating. In b), the EDX maps indicate an additional Al-rich phase at the grain boundaries.

microstructure without any pronounced features in the BF STEM image (Fig. 2e). The DCMS$_{RT, anneal}$ sample, which was deposited without intentional heating and subsequently annealed at *650 °C*, showed an equiaxed microstructure (Fig. 2d).
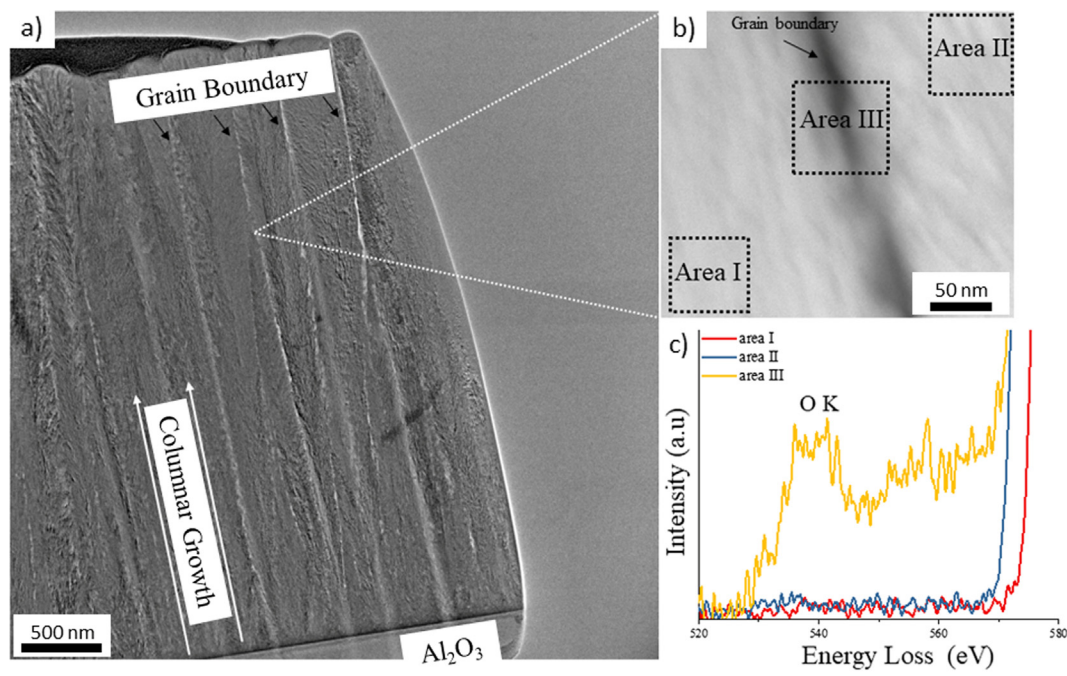
Fig. 4. a) Overview TEM BF image of the investigated coating deposited onto Al_2O_3. b) HAADF STEM image recorded at higher magnification from a grain boundary region as indicated in a). The marked areas reveal positions at which the EELS-spectra were recorded. c) EELS O-K spectra for each area (marked in b) are shown. Only the area containing the grain boundary reveals a significant O-signal.
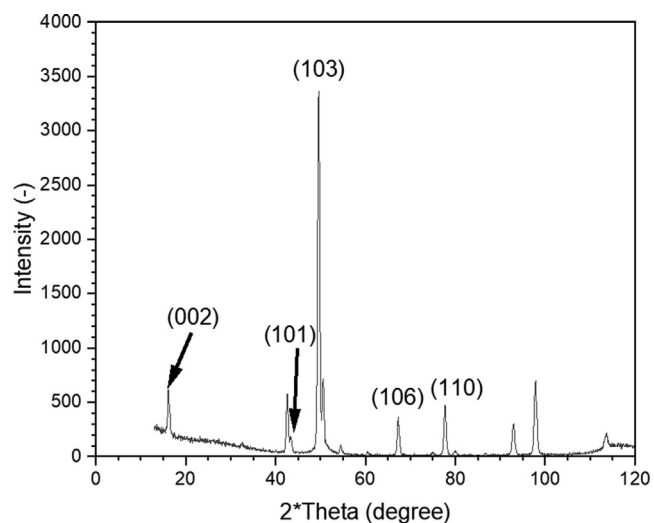

Fig. 5. X-ray diffraction results for the $DCMS_{RT, anneal}$ sample showing the (0 0 2)- and (1 0 1)-peak (indicated by arrows), which suggest the occurrence of the ordered MAX phase crystal structure.

The HAADF images in Fig. 3 support the findings of the BF images of features at the grain boundary for the $DCMS_{565°C}$, $DCMS_{lab, 600°C}$ and the $HPPMS_{565°C}$ sample. For the $DCMS_{RT, as-dep}$ and the $DCMS_{RT, anneal}$ sample no pronounced features are found, they appear to have a homogeneous composition (not shown). Additional EDX measurements confirmed the HAADF findings of a homogeneous composition for both samples deposited without intentional heating. For the samples deposited at elevated substrate temperatures, the EDX maps of Cr and Al shown in Fig. 3 revealed that the features at the grain boundaries for the $DCMS_{565°C}$ and $HPPMS_{565°C}$ samples, Fig. 3a and c respectively, appear to be pores, while the $DCMS_{lab, 600°C}$ sample shows an enrichment of Al at the grain boundary. The O-map is intentionally left out since the O-K and the Cr-L peaks of the EDX spectra are very close to each other and cannot be distinguished in the accuracy of the performed EDX measurements.

The (S)TEM EELS measurements of the Cr_2AlC coating on Al_2O_3 revealed an increased O content at the grain boundary compared to the grain interior. A qualitative comparison of O concentration at the grain boundary and the grain interior is depicted in Fig. 4. revealing an increase of the O-content at the grain boundary region compared to the grain interior.

Table 2
Fracture toughness from the *in situ* micro-bending experiments and the hardness from nanoindentation. Additionally, the estimated yield stress and the minimum required sample size according to Eq. (3) for the fracture toughness experiments, to be valid linear elastic experiments, is listed. The error given for the fracture toughness experiments and the hardness measurement is the standard deviation performed tests for each coating. Furthermore, the observed microstructure is listed.

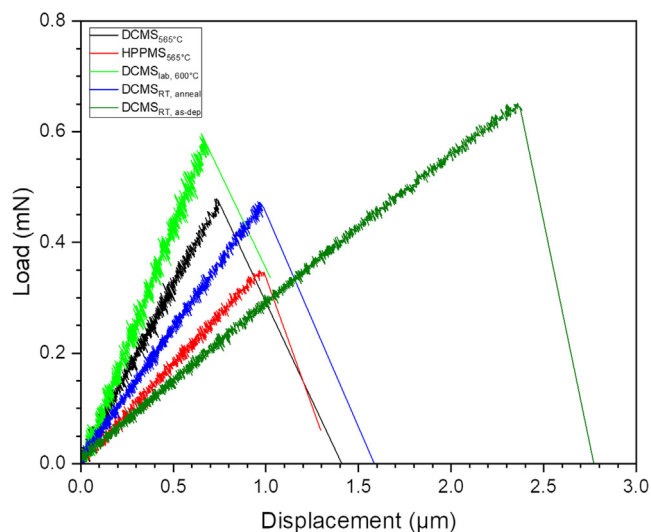| Sample	Fracture Toughness ($MPam^{1/2}$)	Hardness (GPa)	Estimated Yield Strength (GPa)	Minimum Required Sample Size (μm)	Microstructure
$DCMS_{565°C}$	1.8 ± 0.1	8 ± 2	2.7	1.2	Crystalline columnar
$HPPMS_{565°C}$	2.0 ± 0.2	16 ± 2	5.3	0.4	Crystalline columnar
$DCMS_{lab, 600°C}$	2.3 ± 0.1	10 ± 2	3.3	1.2	Crystalline columnar
$DCMS_{RT, anneal}$	2.4 ± 0.2	15 ± 0.4	5.0	0.6	Crystalline equiaxed
$DCMS_{RT, as-dep}$	4.1 ± 0.5	14 ± 0.2	4.7	2.0	amorphous

Fig. 6. Exemplary load–displacement curves for one sample of each coating.

XRD measurements revealed for all the crystalline samples a MAX phase crystal structure, as to be expected for Cr_2AlC. An exemplary diffractogram for the equiaxed $DCMS_{RT, anneal}$ sample is shown in Fig. 5 where the presence of the (002) and (101) peaks, which are marked with arrows, indicate the formation of the MAX phase structure. Both peaks are, in comparison to the disordered solid solution structure, unique to the MAX phase [25].

The results of the *in situ* micro-bending beam experiments are listed in Table 2. All samples show a linear elastic load–displacement curve. This is depicted in Fig. 6 for one sample of each investigated coating.

The given error of the measurements is the standard deviation from the evaluated coatings (five samples for each coating). Fracture toughness changes which are clearly distinguishable (considering the error bars) are referred to as significant, while overlapping error bars between different samples are referred to as minor changes.

The hardness values extracted from the nanoindentation measurements, the estimated yield strengths according to [49] (Eq. (4)) and the minimum required sample dimensions according to Eq. (3) are found for each material in Table 2.

In Fig. 7, SEM images of the fracture surfaces for the investigated coatings are depicted. There, elongated features are found on the surfaces of the $DCMS_{565°C}$ (Fig. 7a) and $HPPMS_{565°C}$ (Fig. 7c) sample. The $DCMS_{lab, 600°C}$ (Fig. 7b) showed some elongated feature, but additionally, a rough appearance of the fracture surface is visible. It was not possible to preserve both fracture surfaces for the $DCMS_{565°C}$, $DCMS_{lab, 600°C}$ and $HPPMS_{565°C}$ coatings. Therefore, one has to be careful with the interpretation of the fractographs. Since all the fracture surfaces, for each individual coating,
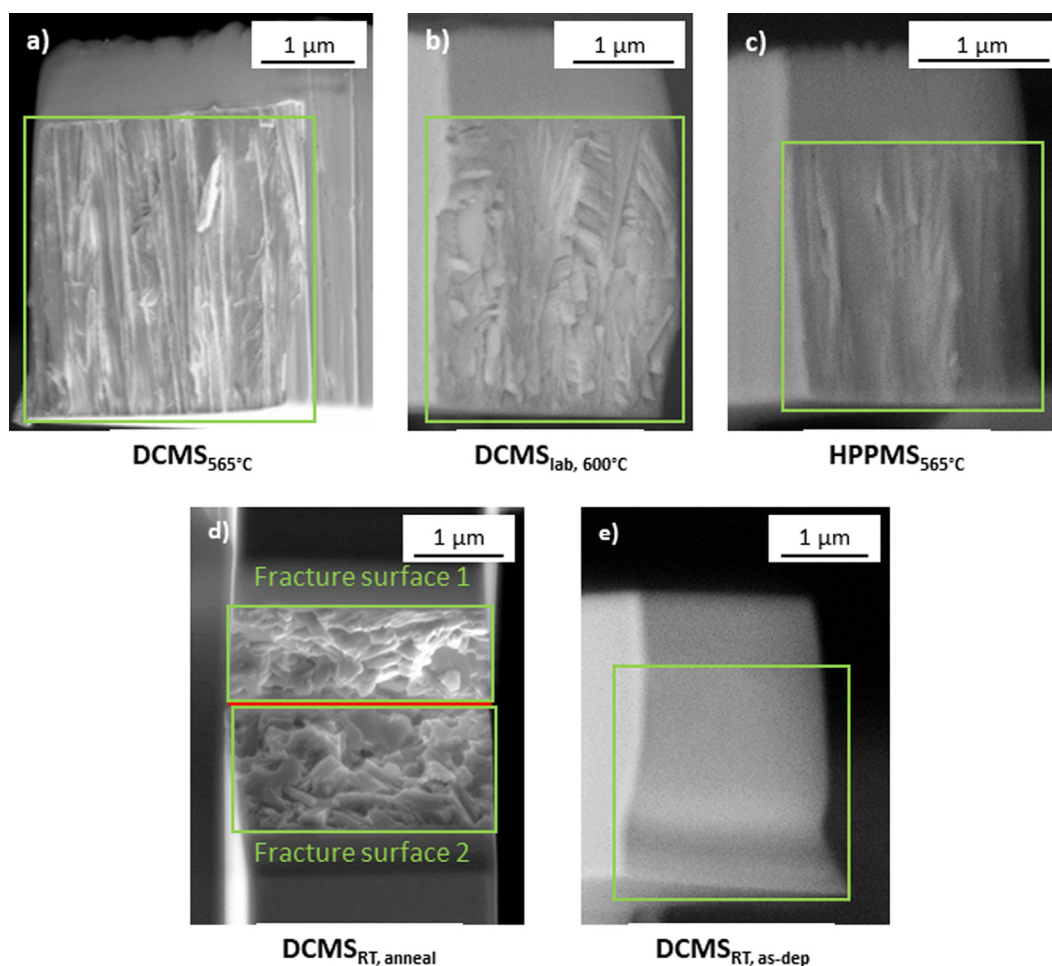

Fig. 7. Fractographs of the a) $DCMS_{565°C}$, b) $DCMS_{lab, 600°C}$, c) $HPPMS_{565°C}$, d) $DCMS_{RT, anneal}$ and e) $DCMS_{RT, as-dep}$. In a), b), c) and e) one side of the fracture surfaces are depicted. The second fracture surface was lost during the *in situ* SEM micromechanical testing. In d) both fracture surfaces are depicted, the red line divides the two fracture surfaces. The green squares highlight the fracture surfaces. Above the fracture surface of each sample, the smooth surface of the pre-notch is visible. (For interpretation of the references to colour in this figure legend, the reader is referred to the web version of this article.)

show similar features, it is assumed that those are representative for the corresponding coating. Fig. 7d depicts a very rough fracture surface for a DCMS$_{RT, anneal}$ sample. In this case, both fracture surfaces could be preserved and one can clearly see the crystalline appearance of the fracture surface. The grains that are pulled out from one side can be found on the other. An exemplary fracture surface for the amorphous material is depicted in Fig. 7e. There are no pronounced features on the fracture surface and it appears to be smooth. Only in the lower part of the fractograph, a kinking of the crack away from the straight through fracture is revealed. This feature is found on all the fracture surfaces for the DCMS$_{RT, as-dep}$ samples and the origin thereof is unclear at this point in time.

4. Discussion

The fracture mechanical results appear surprising, since all the crystalline samples, with different microstructures, reveal only a minor difference in their fracture toughness.

The fracture toughness measured for the investigated crystalline Cr$_2$AlC coatings range from *1.8 to 2.4 MPam$^{1/2}$, which* include the lower limit of *1.9 MPam$^{1/2}$* reported for bulk fine grained material (grain size of around 2 μm) [28].

It has to be pointed out, that a correlative discussion on the morphology affected fracture behavior of Cr$_2$AlC coatings and Cr$_2$AlC bulk materials is flawed by the strongly different grain sizes, which are for the bulk materials at least one order of magnitude larger than the coating thickness.

The DCMS$_{565°C}$ sample, with *1.8 ± 0.1 MPam$^{1/2}$*, is the one with the lowest fracture toughness and the DCMS$_{lab, 600°C}$ and the DCMS$_{RT, anneal}$, with *2.3 ± 0.1 MPam$^{1/2}$* and *2.4 ± 0.2 MPam$^{1/2}$*, respectively, are the ones with the highest fracture toughness. The HPPMS$_{565°C}$ sample is in between those two with a fracture toughness of *2.0 ± 0.2 MPam$^{1/2}$*. Therefore, it is evident, that the synthesis induced differences in crystalline microstructure studied here exhibit only a minor influence on the fracture toughness behavior.

A completely different picture was revealed by the DCMS$_{RT, as-dep}$ sample with the amorphous microstructure. This sample has a fracture toughness of almost twice the one from the crystalline samples (*4.1 ± 0.5 MPam$^{1/2}$*). Such a high fracture toughness is above the limit allowing to use linear elastic fracture mechanics, to determine a sample size independent fracture toughness K_{IC} according to the ASTM E399-90 standard, since the minimum requirements regarding the sample geometry are not met, at least within the constraints (yield strength was estimated via the hardness obtained with nanoindentation) used in this investigation. Hence, the fracture toughness for the DCMS$_{RT, as-dep}$ sample has to be considered a conditional sample size dependent fracture toughness K_Q, not a sample size independent critical mode I fracture toughness (K_{IC}), as for the crystalline samples. In general, there are several open questions regarding measurements of the fracture toughness of amorphous materials with small scale cantilever testing. (i) it is not established how the occurring shear bands are influenced by the strain gradient in the small-scale cantilever upon testing. (ii) another point is raised by Pippan et al. [50] that one has to be careful with the interpretation of small-scale fracture testing results, when the microstructural features are not small compared to the sample dimensions. In the case of an amorphous material, it is not straight forward what to define as microstructural feature. Therefore, one should be careful with the conclusions drawn from micro-bending beam experiments of amorphous materials.

The fracture surfaces of the samples at elevated deposition temperature (DCMS$_{565°C}$, DCMS$_{lab, 600°C}$ and HPPMS$_{565°C}$) show elongated features. This corresponds well to the TEM findings, which revealed a columnar microstructure for these samples. The sample deposited without intentional heating and subsequently annealed

(DCMS$_{RT, anneal}$) has a very rough fracture surface (Fig. 7d), suggesting an equiaxed microstructure, which was confirmed by the STEM BF images (Fig. 2d). A smooth fracture surface without any pronounced features is occurring for the sample deposited at without intentional heating (Fig. 7e). This is corresponding well to the STEM findings of an amorphous crystal structure for this sample (Fig. 2e).

The STEM (HAADF and EDX) investigations explained the minor difference in fracture toughness of the crystalline samples. It was found that the DCMS$_{565°C}$ sample, the one with the lowest fracture toughness, showed several features at the grain boundary in the BF and HAADF STEM images. These features were analyzed in more detail utilizing EDX in the STEM and those features appear to be pores at the grain boundaries. These pores occurred across the entire thickness of the DCMS$_{565°C}$ coating at different grain boundaries of the elongated grains. In case of the HPPMS$_{565°C}$ sample, the pores only occurred in the upper half of the deposited coating. For the lower half of the coating, a dense microstructure was observed. At first sight, the DCMS$_{lab, 600°C}$ showed a similar appearance of pores in the BF and HAADF STEM image as the DCMS$_{565°C}$ sample. However, the EDX analysis revealed, that the features at the grain boundaries in the DCMS$_{lab, 600°C}$ sample are enriched in Al. The EELS measurement performed on a Cr$_2$AlC coating on Al$_2$O$_3$ (similar to the DCMS$_{lab, 600°C}$) suggest that the Al enriched at the grain boundary is occurring in the form of Al-oxide in the DCMS$_{lab, 600°C}$ sample. The DCMS$_{RT, anneal}$ sample did not reveal any pronounced features in the STEM investigation, thus suggesting a dense and homogeneous coating.

Taking all these findings under consideration, the difference in the fracture toughness observed in the investigated crystalline coatings may be explained as follows. The pores observed for the DCMS$_{565°C}$ sample across the entire coating thickness and the HPPMS$_{565°C}$ sample only in the upper half lower the fracture toughness by ~ *20%* compared to the equiaxed-dense coating (DCMS$_{RT, anneal}$). In addition, it is revealed that the Al-oxide segregations, found at the grain boundary of the DCMS$_{lab, 600°C}$ sample, is not detrimental to the fracture toughness of the coating compared to the equiaxed (DCMS$_{RT, anneal}$) microstructure. Furthermore, the SEM images from the fracture surfaces of all crystalline coatings reveal intercrystalline failure along the grain boundaries resulting in similar fracture toughness values and, hence, suggesting the grain boundaries being the preferred crack path for the crystalline material. Therefore, it seems that the type of crystalline microstructure (equiaxed or columnar) has a minor influence on the fracture toughness of the investigated Cr$_2$AlC coatings. It is reasonable to assume that the comparatively low fracture toughness is due to the here identified porosity and/or oxygen segregations at the grain boundaries. Although, it is interesting to note that the fracture toughness values of the here investigated MAX phase Cr$_2$AlC coatings coincide with the lower limit of fracture toughness values reported for bulk fine grained Cr$_2$AlC [28]. Furthermore, atom probe tomography on equiaxed coatings synthesized with identical processing parameters clearly showed the presence of oxygen rich regions [51], which may also have an adverse effect on fracture toughness. It may be speculated that a reduced porosity at the grain boundaries and a reduced oxygen incorporation during synthesis and/or atmosphere exposure may increase the coatings fracture toughness and that the extent of the increase depends on the coating morphology.

5. Conclusions

It was shown that the microstructure does have a minor influence on the critical mode I fracture toughness (K_{IC}) of the here investigated crystalline Cr$_2$AlC coatings with an ordered MAX

phase crystal structure. In contrast to the crystalline coatings, a significantly higher conditional fracture toughness (K_Q) was measured for the amorphous sample. The superior fracture toughness of the amorphous coatings compared to the crystalline coatings may be rationalized based on their inherent lack of weak grain boundaries. Combining the findings from this investigation with the ones from Stelzer et al. [19], where Cr_2AlC phase transformations were tracked by resistivity measurements, it can be concluded that Cr_2-AlC is an extremely interesting choice for application as protective and at the same time self-reporting coating. Since the fracture toughness, differs greatly between crystalline and amorphous phases, as shown here, it is proposed that phase transition induced changes in fracture toughness can be tracked by resistivity measurements.

CRediT authorship contribution statement

B. Völker: Conceptualization, Investigation, Formal analysis, Writing - original draft. **B. Stelzer:** Investigation. **S. Mráz:** Investigation. **H. Rueß:** Investigation. **R. Sahu:** Investigation, Formal analysis. **C. Kirchlechner:** Writing - review & editing. **G. Dehm:** Writing - review & editing. **J.M. Schneider:** Conceptualization, Supervision, Writing - review & editing, Funding acquisition.

Declaration of Competing Interest

The authors declare that they have no known competing financial interests or personal relationships that could have appeared to influence the work reported in this paper.

Acknowledgements

References

[1] M.W. Barsoum, T. El-Raghy, Synthesis and Characterization of a Remarkable Ceramic: Ti_3SiC_2, J. Am. Ceram. Soc. 79 (1996) 1953–1956, https://doi.org/10.1111/j.1151-2916.1996.tb08018.x.

[2] M.W. Barsoum, The $M_{N+1}AX_N$ phases: A new class of solids: Thermodynamically stable nanolaminates, Prog. Solid State Chem. 28 (2000) 201–281, https://doi.org/10.1016/S0079-6786(00)00006-6.

[3] M.W. Barsoum, T. El-Raghy, The MAX Phases: Unique New Carbide and Nitride Materials: Ternary ceramics turn out to be surprisingly soft and machinable, yet also heat-tolerant, strong and lightweight, Am. Sci. 89 (2001) 334–343.

[4] Z. Sun, R. Ahuja, S. Li, J.M. Schneider, Structure and bulk modulus of M_2AlC (M=Ti, V, and Cr), Appl. Phys. Lett. 83 (2003) 899–901, https://doi.org/10.1063/1.1599038.

[5] S.E. Lofland, J.D. Hettinger, K. Harrell, P. Finkel, S. Gupta, M.W. Barsoum, G. Hug, Elastic and electronic properties of select M_2AX phases, Appl. Phys. Lett. 84 (2004) 508–510, https://doi.org/10.1063/1.1641177.

[6] P. Eklund, M. Beckers, U. Jansson, H. Högberg, L. Hultman, The $M_{n+1}AX_n$ phases: Materials science and thin-film processing, Thin Solid Films. 518 (2010) 1851–1878, https://doi.org/10.1016/j.tsf.2009.07.184.

[7] M.W. Barsoum, M. Radovic, Elastic and Mechanical Properties of the MAX Phases, Annu. Rev. Mater. Res. 41 (2011) 195–227, https://doi.org/10.1146/annurev-matsci-062910-100448.

[8] Z.M. Sun, Progress in research and development on MAX phases: a family of layered ternary compounds, Int. Mater. Rev. 56 (2011) 143–166, https://doi.org/10.1179/1743280410Y.0000000001.

[9] W. Tian, P. Wang, G. Zhang, Y. Kan, Y. Li, D. Yan, Synthesis and thermal and electrical properties of bulk Cr_2AlC, Scr. Mater. 54 (2006) 841–846, https://doi.org/10.1016/j.scriptamat.2005.11.009.

[10] J.-P. Palmquist, U. Jansson, T. Seppänen, P.O.Å. Persson, J. Birch, L. Hultman, P. Isberg, Magnetron sputtered epitaxial single-phase Ti_3SiC_2 thin films, Appl. Phys. Lett. 81 (2002) 835–837, https://doi.org/10.1063/1.1494865.

[11] J. Emmerlich, H. Högberg, S. Sasvári, P.O.Å. Persson, L. Hultman, J.-P. Palmquist, U. Jansson, J.M. Molina-Aldareguia, Z. Czigány, Growth of Ti_3SiC_2 thin films by elemental target magnetron sputtering, J. Appl. Phys. 96 (2004) 4817–4826, https://doi.org/10.1063/1.1790571.

[12] R. Mertens, Z. Sun, D. Music, J.M. Schneider, Effect of the Composition on the Structure of Cr-Al-C Investigated by Combinatorial Thin Film Synthesis and ab Initio Calculations, Adv. Eng. Mater. 6 (2004) 903–907, https://doi.org/10.1002/adem.200400096.

[13] O. Wilhelmsson, J.-P. Palmquist, T. Nyberg, U. Jansson, Deposition of Ti_2AlC and Ti_3AlC_2 epitaxial films by magnetron sputtering, Appl. Phys. Lett. 85 (2004) 1066–1068, https://doi.org/10.1063/1.1780597.

[14] H. Högberg, L. Hultman, J. Emmerlich, T. Joelsson, P. Eklund, J.M. Molina-Aldareguia, J.-P. Palmquist, O. Wilhelmsson, U. Jansson, Growth and characterization of MAX-phase thin films, Surf. Coat. Technol. 193 (2005) 6–10, https://doi.org/10.1016/j.surfcoat.2004.08.174.

[15] C. Walter, C. Martinez, T. El-Raghy, J.M. Schneider, Towards Large Area MAX Phase Coatings on Steel, Steel Res. Int. 76 (2005) 225–228, https://doi.org/10.1002/srin.200506000.

[16] M. Beckers, N. Schell, R.M.S. Martins, A. Mücklich, W. Möller, Phase stability of epitaxially grown Ti_2AlN thin films, Appl. Phys. Lett. 89 (2006), https://doi.org/10.1063/1.2335681 074101.

[17] J.M. Schneider, D.P. Sigumonrong, D. Music, C. Walter, J. Emmerlich, R. Iskandar, J. Mayer, Elastic properties of Cr_2AlC thin films probed by nanoindentation and ab initio molecular dynamics, Scr. Mater. 57 (2007) 1137–1140, https://doi.org/10.1016/j.scriptamat.2007.08.006.

[18] A. Abdulkadhim, M. Baben, T. Takahashi, V. Schnabel, M. Hans, C. Polzer, P. Polcik, J.M. Schneider, Crystallization kinetics of amorphous Cr_2AlC thin films, Surf. Coat. Technol. 206 (2011) 599–603, https://doi.org/10.1016/j.surfcoat.2011.06.003.

[19] B. Stelzer, X. Chen, P. Bliem, M. Hans, B. Völker, R. Sahu, C. Scheu, D. Primetzhofer, J.M. Schneider, Remote Tracking of Phase Changes in Cr_2AlC Thin Films by In-situ Resistivity Measurements, Sci. Rep. 9 (2019) 8266, https://doi.org/10.1038/s41598-019-44692-4.

[20] D.E. Hajas, M. Baben, B. Hallstedt, R. Iskandar, J. Mayer, J.M. Schneider, Oxidation of Cr_2AlC coatings in the temperature range of 1230 to 1410°C, Surf. Coat. Technol. 206 (2011) 591–598, https://doi.org/10.1016/j.surfcoat.2011.03.086.

[21] S. Li, L. Xiao, G. Song, X. Wu, W.G. Sloof, S. van der Zwaag, Oxidation and Crack Healing Behavior of a Fine-Grained Cr_2AlC Ceramic, J. Am. Ceram. Soc. 96 (2013) 892–899, https://doi.org/10.1111/jace.12170.

[22] H.J. Yang, Y.T. Pei, J.Th.M. De Hosson, Oxide-scale growth on Cr_2AlC ceramic and its consequence for self-healing, Scr. Mater. 69 (2013) 203–206, https://doi.org/10.1016/j.scriptamat.2013.04.013.

[23] L. Shen, D. Eichner, S. van der Zwaag, C. Leyens, W.G. Sloof, Reducing the erosive wear rate of Cr_2AlC MAX phase ceramic by oxidative healing of local impact damage, Wear. 358–359 (2016) 1–6, https://doi.org/10.1016/j.wear.2016.03.019.

[24] K.G. Pradeep, K. Chang, A. Kovács, S. Sen, A. Marshal, R. de Kloe, R.E. Dunin-Borkowski, J.M. Schneider, Nano-scale Si segregation and precipitation in Cr_2Al(Si)C MAX phase coatings impeding grain growth during oxidation, Mater. Res. Lett. 7 (2019) 180–187, https://doi.org/10.1080/21663831.2019.1572663.

[25] C.J. Gilbert, D.R. Bloyer, M.W. Barsoum, T. El-Raghy, A.P. Tomsia, R.O. Ritchie, Fatigue-crack growth and fracture properties of coarse and fine-grained Ti_3SiC_2, Scr. Mater. 42 (2000) 761–767, https://doi.org/10.1016/S1359-6462(99)00427-3.

[26] S.B. Li, W.B. Yu, H.X. Zhai, G.M. Song, W.G. Sloof, S. van der Zwaag, Mechanical properties of low temperature synthesized dense and fine-grained Cr_2AlC ceramics, J. Eur. Ceram. Soc. 31 (2011) 217–224, https://doi.org/10.1016/j.jeurceramsoc.2010.08.014.

[27] M. Yan, X. Duan, Z. Zhang, X. Liao, X. Zhang, B. Qiu, Z. Wei, P. He, J. Rao, X. Zhang, D. Jia, Y. Zhou, Effect of ball milling treatment on the microstructures and properties of Cr_2AlC powders and hot pressed bulk ceramics, J. Eur. Ceram. Soc. 39 (2019) 5140–5148, https://doi.org/10.1016/j.jeurceramsoc.2019.07.052.

[28] X. Duan, L. Shen, D. Jia, Y. Zhou, S. van der Zwaag, W.G. Sloof, Synthesis of high-purity, isotropic or textured Cr_2AlC bulk ceramics by spark plasma sintering of pressure-less sintered powders, J. Eur. Ceram. Soc. 35 (2015) 1393–1400, https://doi.org/10.1016/j.jeurceramsoc.2014.11.008.

[29] G.M. Pharr, W.C. Oliver, Measurement of Thin Film Mechanical Properties Using Nanoindentation, MRS Bull. 17 (1992) 28–33, https://doi.org/10.1557/S0883769400041634.

[30] W.D. Nix, Elastic and plastic properties of thin films on substrates: nanoindentation techniques, Mater. Sci. Eng. A. 234–236 (1997) 37–44, https://doi.org/10.1016/S0921-5093(97)00176-7.

[31] H. Ljungcrantz, M. Odén, L. Hultman, J.E. Greene, J.-E. Sundgren, Nanoindentation studies of single-crystal (001)-, (011)-, and (111)-oriented TiN layers on MgO, J. Appl. Phys. 80 (1996) 6725–6733, https://doi.org/10.1063/1.363799.

[32] R. Daniel, M. Meindlhumer, J. Zalesak, B. Sartory, A. Zeilinger, C. Mitterer, J. Keckes, Fracture toughness enhancement of brittle nanostructured materials by spatial heterogeneity: A micromechanical proof for CrN/Cr and TiN/SiO_x multilayers, Mater. Des. 104 (2016) 227–234, https://doi.org/10.1016/j.matdes.2016.05.029.

[33] M. Bartosik, C. Rumeau, R. Hahn, Z.L. Zhang, P.H. Mayrhofer, Fracture toughness and structural evolution in the TiAlN system upon annealing, Sci. Rep. 7 (2017) 16476, https://doi.org/10.1038/s41598-017-16751-1.

[34] R. Hahn, M. Bartosik, R. Soler, C. Kirchlechner, G. Dehm, P.H. Mayrhofer, Superlattice effect for enhanced fracture toughness of hard coatings, Scr. Mater. 124 (2016) 67–70, https://doi.org/10.1016/j.scriptamat.2016.06.030.

[35] R. Daniel, M. Meindlhumer, W. Baumegger, J. Todt, J. Zalesak, T. Ziegelwanger, C. Mitterer, J. Keckes, Anisotropy of fracture toughness in nanostructured ceramics controlled by grain boundary design, Mater. Des. 161 (2019) 80–85, https://doi.org/10.1016/j.matdes.2018.11.028.

[36] R. Soler, S. Gleich, C. Kirchlechner, C. Scheu, J.M. Schneider, G. Dehm, Fracture toughness of Mo$_2$BC thin films: Intrinsic toughness versus system toughening, Mater. Des. 154 (2018) 20–27, https://doi.org/10.1016/j.matdes.2018.05.015.

[37] J.S.K.-L. Gibson, S. Rezaei, H. Rueß, M. Hans, D. Music, S. Wulfinghoff, J.M. Schneider, S. Reese, S. Korte-Kerzel, From quantum to continuum mechanics: studying the fracture toughness of transition metal nitrides and oxynitrides, Mater. Res. Lett. 6 (2018) 142–151, https://doi.org/10.1080/21663831.2017.1414081.

[38] K. Matoy, H. Schönherr, T. Detzel, T. Schöberl, R. Pippan, C. Motz, G. Dehm, A comparative micro-cantilever study of the mechanical behavior of silicon based passivation films, Thin Solid Films. 518 (2009) 247–256, https://doi.org/10.1016/j.tsf.2009.07.143.

[39] B.N. Jaya, C. Kirchlechner, G. Dehm, Can microscale fracture tests provide reliable fracture toughness values? A case study in silicon, J. Mater. Res. 30 (2015) 686–698, https://doi.org/10.1557/jmr.2015.2.

[40] M. Sebastiani, K.E. Johanns, E.G. Herbert, F. Carassiti, G.M. Pharr, A novel pillar indentation splitting test for measuring fracture toughness of thin ceramic coatings, Philos. Mag. 95 (2015) 1928–1944, https://doi.org/10.1080/14786435.2014.913110.

[41] S. Liu, J.M. Wheeler, P.R. Howie, X.T. Zeng, J. Michler, W.J. Clegg, Measuring the fracture resistance of hard coatings, Appl. Phys. Lett. 102 (2013) 171907, https://doi.org/10.1063/1.4803928.

[42] D.D. Maio, S.G. Roberts, Measuring fracture toughness of coatings using focused-ion-beam-machined microbeams, J. Mater. Res. 20 (2005) 299–302, https://doi.org/10.1557/JMR.2005.0048.

[43] M. Faleschini, H. Kreuzer, D. Kiener, R. Pippan, Fracture toughness investigations of tungsten alloys and SPD tungsten alloys, J. Nucl. Mater. 367–370, Part A (2007) 800–805, https://doi.org/10.1016/j.jnucmat.2007.03.079.

[44] F. Wetscher, R. Stock, R. Pippan, Changes in the mechanical properties of a pearlitic steel due to large shear deformation, Mater. Sci. Eng. A. 445–446 (2007) 237–243, https://doi.org/10.1016/j.msea.2006.09.026.

[45] A. Hohenwarter, R. Pippan, Anisotropic fracture behavior of ultrafine-grained iron, Mater. Sci. Eng. A. 527 (2010) 2649–2656, https://doi.org/10.1016/j.msea.2009.12.033.

[46] I. Sabirov, R.Z. Valiev, I.P. Semenova, R. Pippan, Effect of equal channel angular pressing on the fracture behavior of commercially pure titanium, Metall. Mater. Trans. A. 41 (2010) 727–733, https://doi.org/10.1007/s11661-009-0111-z.

[47] S. Brinckmann, K. Matoy, C. Kirchlechner, G. Dehm, On the influence of microcantilever pre-crack geometries on the apparent fracture toughness of brittle materials, Acta Mater. 136 (2017) 281–287, https://doi.org/10.1016/j.actamat.2017.07.014.

[48] ASTM E399-90. Standard test method for plane-strain fracture toughness of metallic materials, American Society of Testing and Materials, Philadelphia (PA), 1990.

[49] D. Tabor, The Hardness of Metals, Clarendon Press, Oxford, UK, 1951.

[50] R. Pippan, S. Wurster, D. Kiener, Fracture mechanics of micro samples: Fundamental considerations, Mater. Des. 159 (2018) 252–267, https://doi.org/10.1016/j.matdes.2018.09.004.

[51] X. Chen, B. Stelzer, M. Hans, R. Iskandar, J. Mayer, J.M. Schneider, Enhancing the high temperature oxidation behavior of Cr$_2$AlC coatings by reducing grain boundary nanoporosity, Mater. Res. Lett. 9 (2021) 127–133, https://doi.org/10.1080/21663831.2020.1854358.